Design of simultaneous high-*Q* and high-sensitivity photonic crystal refractive index sensors

Daquan Yang,[1,2] Huiping Tian,[2,3] Yuefeng Ji,[2] and Qimin Quan[1,*]

[1]Rowland Institute at Harvard University, Cambridge, Massachusetts 02142, USA
[2]State Key Laboratory of Information Photonics and Optical Communications, School of Information and Communication Engineering, Beijing University of Posts and Telecommunications, Beijing 100876, China
[3]Key Laboratory of Micro and Nano Photonic Structures (Ministry of Education), and State Key Laboratory of Surface Physics, Fudan University, Shanghai 200433, China
*Corresponding author: quan@rowland.harvard.edu

Received February 28, 2013; revised June 5, 2013; accepted June 5, 2013; posted June 5, 2013 (Doc. ID 185836); published July 3, 2013

Sensitivities (S) and quality factors (Q) have been trade-offs in label-free optical resonator sensors, and optimal geometry that maximizes both factors is under active development. In this paper, we demonstrate that the nanoslotted parallel multibeam cavity possesses unexplored high S and high Q. We achieve $S > 800$ nm/RIU (refractive index unit) and $Q > 10^7$ in liquid at telecom wavelength range when absorption is neglected. To the best of our knowledge, this is the first geometry that features both high S and Q factors, and thus is potentially an ideal platform for refractive index-based biochemical sensing.

OCIS codes: (130.3120) Integrated optics devices; (230.5298) Photonic crystals; (230.5750) Resonators; (280.4788) Optical sensing and sensors.
http://dx.doi.org/10.1364/JOSAB.30.002027

1. INTRODUCTION

Optical resonances have been widely used in biomedical label-free sensors [1–3]. The most exploited schemes are based on the principle of surface plasmon resonance [4–6], interferometry [7–9], and optical cavities [10–18]. Among these, photonic crystal (PhC) cavities show advantages in integrated lab-on-chip devices due to the small footprints and high integrability with optical circuits [19,20]. A variety of optical cavity sensors based on PhC waveguides, 2D PhC slabs, and 1D nanobeam PhC cavities have been demonstrated [21–30]. The figure of merit (FOM) of these sensors can be defined as $\mathrm{FOM} = S \cdot Q/\lambda_{\mathrm{res}}$ [31], where S is the shift of resonance in response to the surrounding index change, λ_{res} is the cavity resonance, and Q is the quality factor of the cavity. However, the trade-off between S and Q limits the FOM: to achieve high S, the optical mode needs to overlap strongly with the detecting target (i.e., outside of the waveguiding medium), yet in order to achieve a higher Q, the optical mode should be more localized in the waveguiding medium. Here, an extensive comparison between different sensing systems is summarized in Table 1. As seen, PhC-based sensors have overall larger FOMs. The optimized S's of most PhC geometries are generally around $100 \sim 300$ nm/RIU (RIU = refractive index unit) at around 1550 nm wavelength [22–30]. It is found that "slot" structure [36,37]—the nanosize low index gap between high index waveguides—can greatly enhance S while maintaining the same level of Q. S in a slotted cavity is enhanced generally by twice ($S \sim 500$ nm/RIU) its nonslotted counterpart [38–42]. In particular, di Falco *et al.* [43] demonstrated S of 1538 nm/RIU in a slot heterostructure cavity, and Wang *et al.* [44,45] demonstrated S of 900 nm/RIU in slot double-beam waveguides/cavities. However, Q factors are limited to 4000 in [43] and 700 in [44]. In this paper, we propose the nanoslotted parallel multibeam cavity (NPMC). We demonstrated that a NPMC sensor can possess ultrahigh S exceeding 800 nm/RIU (at 1531 nm) and Q exceeding 10^7. Taking water absorption into consideration at telecom wavelength range, Q of the sensor will be limited to 10^4 [30,46], resulting in FOM of ~5000. This is, to the best of our knowledge, the first photonic structure that has simultaneously ultrahigh Q and S.

2. NANOSLOTTED PARALLEL MULTIBEAM CAVITY

The schematics of the NPMC are shown in Fig. 1. They consist of multiple parallel PhC nanobeam cavities [12] with nanogap separations. The gratings are the rectangular shapes in Fig. 1, but we found that circular gratings can achieve similar performance. The cavity design follows our recently discovered deterministic high-Q recipe [16,17]. Hence the center-to-center distance of the rectangular gratings are the same (defined as "periodicity" a), and the widths of the gratings $[w_x(i)]$ are tapered in a quadratic manner. A key advantage of this method in the current application is that the cavity resonance can be predicted by the band-edge frequency of its unit cell in the center of the cavity. Therefore, the resonance shift in response to different refractive index background (i.e., S factor) can be obtained from computationally low-cost band-diagram simulations.

3. OPTIMIZE SENSITIVITY IN THE NANOSLOTTED PARALLEL MULTIBEAM CAVITY

In order to compare the sensitivity of the cavities at different resonances, we define normalized sensitivity as

Table 1. Sensitivity, *Q* Factor, and FOM of Various Optical Sensing Schemes

Sensing System		Sensitivity (nm/RIU)	*Q* Factor in Water (At Telecom Range)	FOM	Ref.
Interferometry	MZI[a]	~2000	~500	~645	[7]
WGM[b] based	Microdisk	~70	$\sim 10^3$	~45	[32]
	Microring	70–200	$\sim 10^3$	45–142	[33–35]
PhC based	1D nanobeam	~100	$\sim 10^4$	~645	[30]
	2D slab	100–300	10^3–10^4	200–645	[22–28]
	PhC slot	490–1500	$\sim 10^3$	300–1000	[41–45]

[a]Mach–Zehnder interferometer.
[b]Whispering-gallery mode.

$S_{\text{norm}} = S/\lambda_{\text{res}}$. The multibeams are made of silicon, and the surrounding media have indices that vary around the index of common liquid at telecom wavelength ($n_{\text{si}} = 3.46$, $n_{\text{liquid}} = 1.315$). The thickness of the beam is 220 nm. In the following discussion and simulation, we only consider the TE-polarized modes, as the TM band does not have a bandgap at small beam thickness. From the band-diagram calculation, we obtained S_{norm} versus N_{nb} [as shown in Fig. 2(a)]. The sensitivity increases by 4 as N_{nb} increases from 1 to 4 and gradually saturates beyond $N_{\text{nb}} = 4$. This result is also valid for different $\sum_{wvg}/\sum_{\text{slot}}$ proportions. $\sum_{wvg}$ represents the sum of all nanobeam widths ($\sum_{wvg} = b \times N_{\text{nb}}$), and $\sum_{\text{slot}}$ represents the sum of all slot widths [$\sum_{\text{slot}} = w \times (N_{\text{nb}} - 1)$]. For instance, when $\sum_{wvg}/\sum_{\text{slot}} = 8/3$, the normalized sensitivity is as high as 0.583 at $N_{\text{nb}} = 6$. This translates S of 903 nm/RIU at 1550 nm resonance wavelength. To explain this phenomena, we simulated the TE-like mode and the major field (E field in plane, perpendicular to the beams) distribution of the NPMC for $N_{\text{nb}} = 1, 2, 3, 4, 5$, and 6 at $\sum_{wvg}/\sum_{\text{slot}} = 8/3$ [Fig. 2(b)]. The red dashed lines indicate the structure. The optical field is mainly localized in silicon when $N_{\text{nb}} = 1$. As N_{nb} increases, light is forced into the slot region as a result of the refractive index discontinuity [36,37]. When $N_{\text{nb}} \geq 4$, most light has been strongly squeezed in the slot region, and thus, high S is achieved. In Fig. 2(c), we summarized the normalized sensitivity versus other geometrical parameters, including periodicity a, single beam width b, slot width w, and the central rectangular hole length w_x and width w_y. We conclude that N_{nb} is the most critical reason for high S.

Next, we designed a high-*Q* cavity based on the quadrabeam ($N_{\text{nb}} = 4$) configuration, since S begins to saturate at $N_{\text{nb}} = 4$. The design process is introduced in detail in

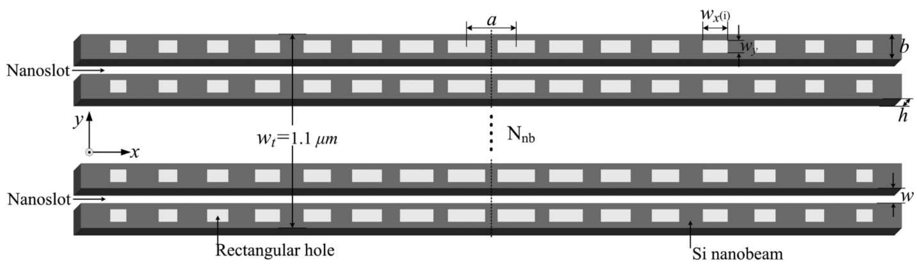

Fig. 1. Schematics of the NPMC that consists of multiple waveguides with nanoslot separations. The structure is symmetric with respect to its center (dashed line). N_{nb} is the number of beams, a is the center-to-center distance between the gratings (periodicity), b, h are the width and thickness of each beam, and w is the width of the nanoslot between adjacent beams. $w_x(i)$ are the lengths of the gratings that are tapered quadratically from center to both ends; w_y is the width of the grating and is kept constant.

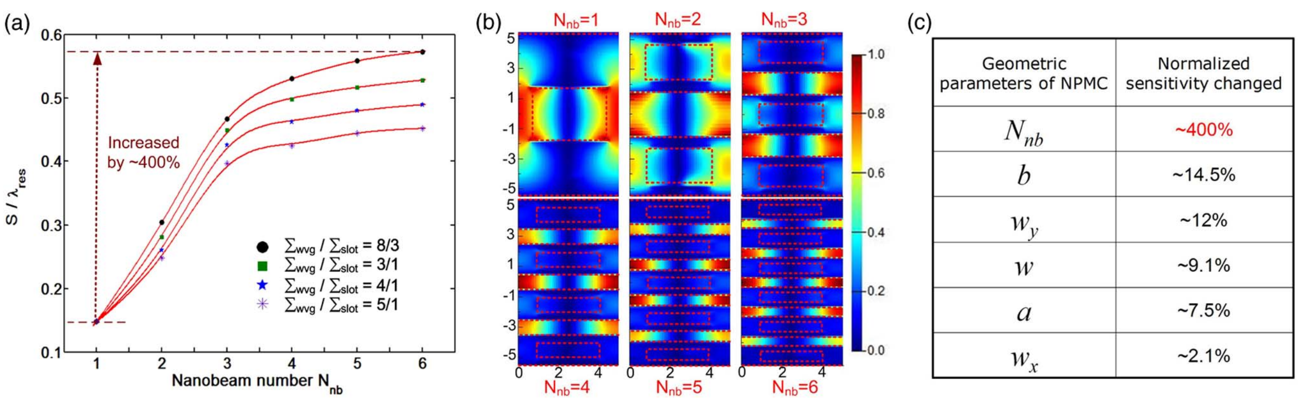

Fig. 2. (a) Normalized sensitivity (S/λ_{res}) as a function of the number of nanobeams N_{nb} when the proportion of $\sum_{wvg}/\sum_{\text{slot}}$ is 5/1, 4/1, 3/1, and 8/3, respectively. The total width of the multibeam structure is kept constant [$w_t = b \times N_{\text{nb}} + w \times (N_{\text{nb}} - 1) = 1.1$ μm]. (b) FDTD simulation of the major field profile (E field in plane, perpendicular to the beams) distribution when $N_{\text{nb}} = 1, 2, 3, 4, 5$, and 6 at $\sum_{wvg}/\sum_{\text{slot}} = 8/3$. Unit of the x/y axis is μm. (c) General change of the normalized sensitivity as different parameters change including the number of beams (N_{nb}), width of each single nanobeam b, width of rectangular grating w_y, width of slot w, periodicity a, and the length of rectangular grating w_x.

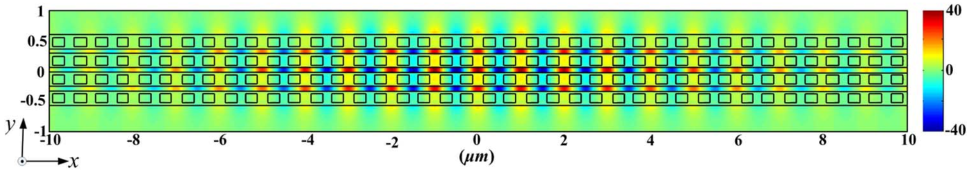

Fig. 3. 3D FDTD simulation of the major field distribution profile (Ey) in the NPMC. Here the number of Gaussian mirror segments $N_{\mathrm{taper}} = 40$, with an additional 20 mirrors on both ends of the tapering section. The calculated Q factor is 3.2×10^7 and the S factor is 808.7 nm/RIU. $w_t = 1.1$ μm, $a = 500$ nm, $b = 200$ nm, $w = 100$ nm, $h = 220$ nm, $w_x(1) = 300$ nm, $w_y = 140$ nm, $w_x(i) = w_x(1) + (i - 1)^2(w_x(i) - w_x(1))/(i_{\max} - 1)^2$, $I = 1, 2 \ldots 40$, and $n_{\mathrm{si}} = 3.46$, $n_{\mathrm{water}} = 1.315$. Unit of the x/y axis is μm.

[16,17]. The thickness of the cavity is 220 nm, periodicity $a = 500$ nm, the nanobeam width $b = 200$ nm, the slot width w between adjacent nanobeams equals 100 nm, and the total width of the NPMC is 1.1 μm. The rectangular gratings are quadratically tapered from $w_{x\text{-start}} = 300$ nm to $w_{x\text{-end}} = 225$ nm, i.e., $w_x(i) = w_x(1) + (i - 1)^2(w_x(i) - w_x(1))/(i_{\max} - 1)^2$ (i increases from 1 to $i_{\max}$). $w_{x\text{-end}} = 225$ nm is obtained from band-diagram simulation, at which maximum mirror strength [16] is achieved. The final cavity structure is symmetric to its center, and on each side, there are 40 gratings ($i_{\max} = 40$) in the Gaussian mirror region [16] and an additional 20 segments that have the same dimension as the last grating in the Gaussian mirror region. The total Q factor is 3.2×10^7 and resonance is at 1531.159 nm obtained from 3D finite-difference time-domain (FDTD) simulation. Figure 3 shows the field profile. It is clearly seen that the optical field is strongly localized in the slotted region. We also calculated S in the full cavity structure and obtained $S = 808.7$ nm/RIU. This agrees very well with $S = 810.2$ nm/RIU obtained from the band-diagram simulation. In addition, we also consider the effect of the fabrication roughness (e.g., sidewall roughness) in our design. Our simulation was done in a water environment (neglecting water absorption), assuming a random distribution of roughness from 0–5, 0–10, 0–15, and 0–20 nm, respectively. It can be seen from Fig. 4 that Q of 10^4–10^5 is achievable with fabrication accessible quality. If the water absorption is taken into account, the absorption Q is limited to the order of 10^4 [30,46] at telecom wavelength range. To further increase Q, water can be replaced by deuterium water (that has same refractive index but weaker absorption in telecom range) as the carrier fluid for sensing applications.

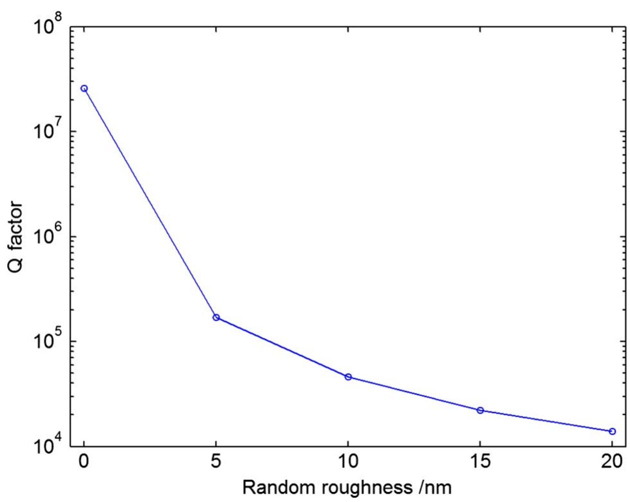

Fig. 4. Effect of fabrication roughness to the Q factors. A random distribution of roughness from 0–5, 0–10, 0–15, and 0–20 nm, respectively, are simulated. The cavity is immersed in an environment with a refractive index of 1.315.

4. NANOSLOTTED PARALLEL MULTIBEAM CAVITY SENSOR

The above NPMC sensor can be easily excited with resonant scattering [15] from a microscope. Alternatively, NPMCs can also be coupled to on-chip optical networks for higher integration and multiplex detection. Therefore, we carried out a coupler design in Fig. 5 inspired by [47]. The coupler consists of a bus waveguide with width $w_C = 900$ nm, and three triangular fingers extruding to the NPMC. Each beam of the NPMC is also tapered in a triangle shape that "bites" with the coupler. Here $w_{\mathrm{taper}} = 300$ nm. The taper angle in the coupler is the same as that in the NPMC. The thickness is kept at 220 nm. The lengths of the taper in the NPMC and in the coupler are $L_{\mathrm{taper}}^{\mathrm{NPMC}} (= 10$ μm) and $L_{\mathrm{taper}}^{\mathrm{coupler}} (= 15$ μm), respectively. With 3D FDTD simulation, we obtained the transmission of the NPMC, as light is launched from the bus waveguide (fundamental TE-like mode) coupled into the NPMC by the above-designed coupler and finally collected from the output bus waveguide. In order to save the simulation time of the transmission calculation, we used a high transmission but low Q geometry: the number of gratings was chosen to be $N_{\mathrm{taper}} = 30$, and there

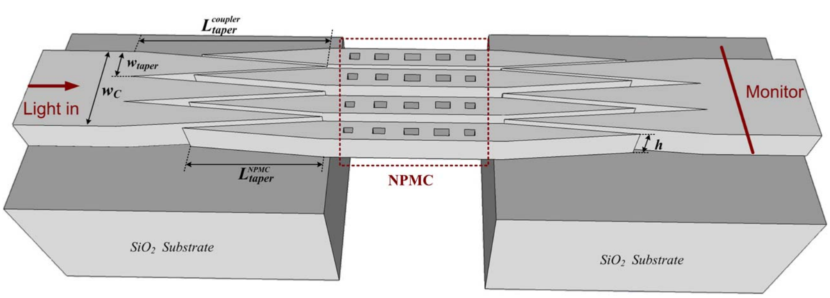

Fig. 5. Schematic diagram of the coupler used for the NPMC sensor in/out coupling. The dark red dashed line area represents the cavity. The structure is symmetric with respect to its center.

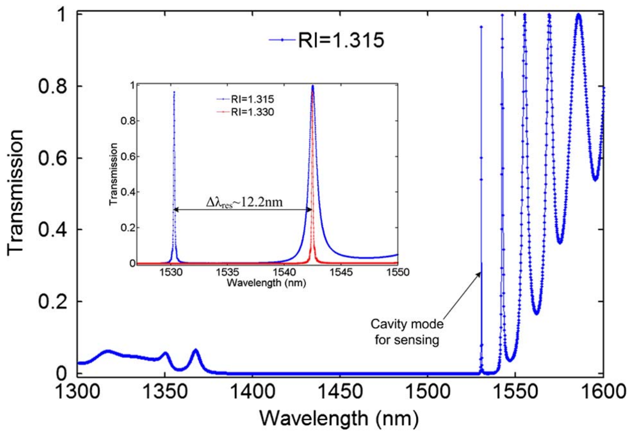

Fig. 6. Transmission spectrum of the NPMC sensor from 3D FDTD simulation. The simulation consists of a bus waveguide with width $w_C = 900$ nm, three triangular fingers extruding to the NPMC, and the NPMC with a total number of gratings $n_{\text{taper}} = 30$. The width of each taper $w_{\text{taper}} = 300$ nm, length of the taper $L_{\text{taper}}^{\text{NPMC}} = 10$ μm, and $L_{\text{taper}}^{\text{coupler}} = 15$ μm. The background refractive index is set as RI = 1.315. A Q of 1.5×10^4 and near unit transmission is obtained. Inset shows the shift of the cavity resonance as the background index changes from RI = 1.315 to RI = 1.330.

were no additional mirrors outside of the Gaussian mirror region. The total transmission spectrum is shown in Fig. 6. A high Q around 1.5×10^4 and near 100% transmission were obtained. The transmission loss includes loss from the coupler. The modes at wavelengths lower than 1380 nm and higher than 1540 nm are the band edge modes. The inset shows the shift of the fundamental mode when the background index changes from RI = 1.315 to RI = 1.330. The resonant wavelength shifted 12.2 nm. Therefore, sensitivity S is 813.3 nm/RIU, which agrees very well with our previous analysis from the band-diagram calculation (810.2 nm/RIU). We note that the current transmission-limited Q factor can be further improved at the cost of reducing the on-resonance transmission. As water is used as the carrier fluid in most of the sensing applications, the absorption of water at telecom wavelength imposes a limitation to the total Q of the sensor to the order of 10^4 [46]. Therefore, this current design has sufficient high Q. Total Q can be further increased by using deuterium water as the carrier fluid.

5. CONCLUSION

Q factors and S factors have been trade-offs in optical resonator sensors. Nevertheless, we demonstrated both record high Q and record high S factors in the NPMCs. We demonstrated $S > 800$ nm/RIU and $Q > 10^7$ with 3D FDTD simulation in the quadrabeam geometry. We also demonstrated that NPMCs can be strongly coupled to the feeding waveguide with near unity transmission with a bus-waveguide-to-NPMC coupler. Therefore, NPMCs can be easily interfaced with both free space optics (with resonant scattering) and on-chip optical circuits (with waveguide couplers), making it an ideal system for label-free sensing applications.

ACKNOWLEDGMENTS

This research was supported by the Rowland Institute at Harvard. The authors greatly appreciate helpful comments from Professor M. Loncar at Harvard University. D. Yang acknowledges the support by the National 973 Program (No. 2012CB315705), National 863 Program (No. 2011AA010303), and the BUPT Excellent Ph.D. Students Foundation (CX201212), China. D. Yang thanks the China Scholarship Council (CSC) (No. 201206470026) for fellowship support.

REFERENCES

1. X. Fan, I. M. White, S. I. Shopova, H. Zhu, J. D. Suter, and Y. Sun, “Sensitive optical biosensors for unlabeled targets: a review,” Anal. Chim. Acta **620**, 8–26 (2008).
2. C. A. Barrios, M. Bauls, V. G. Pedro, K. B. Gylfason, B. Snchez, A. Griol, A. Maquieira, H. Sohlstrm, M. Holgado, and R. Casquel, “Label-free optical biosensing with slot-waveguides,” Opt. Lett. **33**, 708–710 (2008).
3. H. K. Hunt and A. M. Armani, “Label-free biological and chemical sensors,” Nanoscale **2**, 1544–1559 (2010).
4. J. N. Anker, W. P. Hall, O. Lyandres, N. C. Shah, J. Zhao, and R. P. Duyne, “Biosensing with plasmonic nanosensors,” Nat. Mater. **7**, 442–453 (2008).
5. R. Karlsson, “SPR for molecular interaction analysis: a review of emerging application areas,” J. Mol. Recognit. **17**, 151–161 (2004).
6. C. Caucheteur, Y. Shevchenko, L. Shao, M. Wuilpart, and J. Albert, “High resolution interrogation of tilted fiber grating SPR sensors from polarization properties measurement,” Opt. Express **19**, 1656–1664 (2011).
7. J. Yang, L. Jiang, S. Wang, B. Li, M. Wang, H. Xiao, Y. Lu, and H. Tsai, “High sensitivity of taper-based Mach–Zehnder interferometer embedded in a thinned optical fiber for refractive index sensing,” Appl. Opt. **50**, 5503–5507 (2011).
8. A. Ymeti, J. Greve, P. V. Lambeck, T. Wink, S. van Hovell, T. A. M. Beumer, R. R. Wijn, R. G. Heideman, V. Subramaniam, and J. S. Kanger, “Fast, ultrasensitive virus detection using a young interferometer sensor,” Nano Lett. **7**, 394–397 (2007).
9. A. Ymeti, J. S. Kanger, J. Greve, G. A. Besselink, P. V. Lambeck, R. Wijn, and R. G. Heideman, “Integration of microfluidics with a four-channel integrated optical Young interferometer immunosensor,” Biosens. Bioelectron. **20**, 1417–1421 (2005).
10. F. Vollmer and S. Arnold, “Whispering-gallery-mode biosensing: label-free detection down to single molecules,” Nat. Methods **5**, 591–596 (2008).
11. C. Kang and S. M. Weiss, “Photonic crystal with multiple-hole defect for sensor applications,” Opt. Express **16**, 18188–18193 (2008).
12. P. B. Deotare, M. W. McCutcheon, I. W. Frank, M. Khan, and M. Loncar, “High quality factor photonic crystal nanobeam cavities,” Appl. Phys. Lett. **94**, 121106 (2009).
13. P. B. Deotare, M. W. McCutcheon, I. W. Frank, M. Khan, and M. Loncar, “Coupled photonic crystal nanobeam cavities,” Appl. Phys. Lett. **95**, 031102 (2009).
14. K. Foubert, L. Lalouat, B. Cluzel, E. Picard, D. Peyrade, F. Fornel, and E. Hadji, “An air-slotted nanoresonator relying on coupled high Q small V Fabry–Perot nanocavities,” Appl. Phys. Lett. **94**, 251111 (2009).
15. B. Cluzel, K. Foubert, L. Lalouat, E. Picard, J. Dellinger, D. Peyrade, F. Fornel, and E. Hadji, “Optical field molding within near-field coupled twinned nanobeam cavities,” in *Integrated Photonics Research, Silicon and Nanophotonics*, Toronto, Canada, 12 June, 2011.
16. Q. Quan, P. B. Deotare, and M. Loncar, “Photonic crystal nanobeam cavity strongly coupled to the feeding waveguide,” Appl. Phys. Lett. **96**, 203102 (2010).
17. Q. Quan and M. Loncar, “Deterministic design of wavelength scale, ultra-high Q photonic crystal nanobeam cavities,” Opt. Express **19**, 18529–18542 (2011).
18. E. Kuramochi, H. Taniyama, T. Tanabe, K. Kawasaki, Y.-G. Roh, and M. Notomi, “Ultrahigh-Q one-dimensional photonic crystal nanocavities with modulated mode-gap barriers on SiO_2 claddings and on air claddings,” Opt. Express **18**, 15859–15869 (2010).

19. D. Psaltis, S. R. Quake, and C. Yang, "Developing optofluidic technology through the fusion of microfluidics and optics," Nature **442**, 381–386 (2006).
20. C. Monat, P. Domachuk, and B. J. Eggleton, "Integrated optofluidics: a new river of light," Nat. Photonics **1**, 106–114 (2007).
21. J. Topolancik, P. Bhattacharya, J. Sabarinathan, and P.-C. Yu, "Fluid detection with photonic crystal-based multichannel waveguides," Appl. Phys. Lett. **82**, 1143–1145 (2003).
22. M. Loncar, A. Scherer, and Y. Qiu, "Photonic crystal cavity laser sources for chemical detection," Appl. Phys. Lett. **82**, 4648–4651 (2003).
23. E. Chow, A. Grot, I. W. Mirkarimi, M. Sigalas, and G. Girolami, "Ultracompact biochemical sensor built with two-dimensional photonic crystal microcavity," Opt. Lett. **29**, 1093–1095 (2004).
24. T. Xu and N. Zhu, "Pillar-array based optical sensor," Opt. Express **18**, 5420–5425 (2010).
25. Q. Quan, I. B. Burgess, S. K. Y. Tang, D. L. Floyd, and M. Loncar, "High-*Q*, low index-contrast polymeric photonic crystal nanobeam cavities," Opt. Express **19**, 22191–22197 (2011).
26. K. Yao and Y. Shi, "High-*Q* width modulated photonic crystal stack mode-gap cavity and its application to refractive index sensing," Opt. Express **20**, 27039–27044 (2012).
27. C. Kang, C. T. Phare, Y. A. Vlasov, S. Assefa, and S. M. Weiss, "Photonic crystal slab sensor with enhanced surface area," Opt. Express **18**, 27930–27937 (2010).
28. D. Yang, H. Tian, and Y. Ji, "Nanoscale photonic crystal sensor arrays on monolithic substrates using side-coupled resonant cavity arrays," Opt. Express **19**, 20023–20034 (2011).
29. W. Lai, S. Chakravarty, Y. Zou, and R. T. Chen, "Silicon nano-membrane based photonic crystal microcavities for high sensitivity bio-sensing," Opt. Lett. **37**, 1208–1210 (2012).
30. Q. Quan, F. Vollmer, I. B. Burgess, P. B. Deotare, I. W. Frank, T. Sindy, K. Y. Tang, R. Illic, and M. Loncar, "Ultrasensitive on-chip photonic crystal nanobeam sensor using optical bistability," in *Quantum Electronics and Laser Science Conference (QELS)*, Baltimore, Maryland, 1 May, 2011.
31. L. J. Sherry, S. Chang, G. C. Schatz, and R. P. Van Duyne, "Localized surface plasmon resonance spectroscopy of single silver nanocubes," Nano Lett. **5**, 2034–2038 (2005).
32. S. Cho and N. Jokerst, "A polymer microdisk photonic sensor integrated onto silicon," IEEE Photon. Technol. Lett. **18**, 2096–2098 (2006).
33. C. A. Barrios, K. B. Gylfason, B. Snchez, A. Griol, H. Sohlstrm, M. Holgado, and R. Casquel, "Slot-waveguide biochemical sensor," Opt. Lett. **32**, 3080–3082 (2007).
34. K. de Vos, I. Bartolozzi, E. Schacht, P. Bienstman, and R. Baets, "Silicon-on-insulator microring resonator for sensitive and label-free biosensing," Opt. Express **15**, 7610–7615 (2007).
35. C. Chao, W. Fung, and L. Guo, "Polymer microring resonators for biochemical sensing ppplications," IEEE J. Sel. Top. Quantum Electron. **12**, 134–142 (2006).
36. V. R. Almeida, Q. Xu, C. A. Barrios, and M. Lipson, "Guiding and confining light in void nanostructure," Opt. Lett. **29**, 1209–1211 (2004).
37. Q. Quan, I. Bulu, and M. Loncar, "A broadband waveguide QED system on chip," Phys. Rev. A **80**, 011810(R) (2009).
38. F. DellOlio and V. M. N. Passaro, "Optical sensing by optimized silicon slot waveguides," Opt. Express **15**, 4977–4993 (2007).
39. S. Kita, K. Nozaki, and T. Baba, "Refractive index sensing utilizing a cw photonic crystal nanolaser and its array configuration," Opt. Express **16**, 8174–8180 (2008).
40. S. Kita, S. Hachuda, K. Nozaki, and T. Baba, "Nanoslot laser," Appl. Phys. Lett. **97**, 161108 (2010).
41. J. Jgersk, H. Zhang, Z. Diao, N. Le Thomas, and R. Houdré, "Refractive index sensing with an air-slot photonic crystal nanocavity," Opt. Lett. **35**, 2523–2525 (2010).
42. M. G. Scullion, A. di Falco, and T. F. Krauss, "Slotted photonic crystal cavities with integrated microfluidics for biosensing applications," Biosens. Bioelectron. **27**, 101–105 (2011).
43. A. di Falco, L. O'Faolain, and T. F. Krauss, "Chemical sensing in slotted photonic crystal heterostructure cavities," Appl. Phys. Lett. **94**, 063503 (2009).
44. B. Wang, M. A. Dündar, R. Nötzel, F. Karouta, S. He, and R. W. van der Heijden, "Photonic crystal slot nanobeam slow light waveguides for refractive index sensing," Appl. Phys. Lett. **97**, 151105 (2010).
45. B. Wang, M. A. Dündar, R. Nötzel, F. Karouta, S. He, and R. W. van der Heijden, "InGaAsP photonic crystal slot nanobeam waveguides for refractive index sensing," Proc. SPIE **7946**, 79461C (2011).
46. A. M. Armani and K. J. Vahala, "Heavy water detection using ultra-high-*Q* microcavities," Opt. Lett. **31**, 1896–1898 (2006).
47. Z. Wang, N. Zhu, Y. Tang, L. Wosinski, D. Dai, and S. He, "Ultracompact low-loss coupler between strip and slot waveguides," Opt. Lett. **34**, 1498–1500 (2009).